

**RELIABILITY AND DC/RF STRESS INDUCED
DEGRADATION IN InAlGaN/GaN HEMTS FOR RF AND
TERAHERTZ APPLICATIONS**

SHIVANSH AWASTHI



CENTRE FOR APPLIED RESEARCH IN ELECTRONICS

INDIAN INSTITUTE OF TECHNOLOGY DELHI

March 2026

© Indian Institute of Technology Delhi (IITD) New Delhi 2026

**RELIABILITY AND DC/RF STRESS INDUCED
DEGRADATION IN InAlGaN/GaN HEMTS FOR RF AND
TERAHERTZ APPLICATIONS**

by

SHIVANSH AWASTHI

CENTRE FOR APPLIED RESEARCH IN ELECTRONICS

Submitted

in fulfilment of the requirements of the degree of Doctor of Philosophy

to the



INDIAN INSTITUTE OF TECHNOLOGY DELHI

March 2026

CERTIFICATE

This is to certify that the thesis entitled, “**RELIABILITY AND DC/RF STRESS INDUCED DEGRADATION IN InAlGaN/GaN HEMTS FOR RF AND TERAHERTZ APPLICATIONS**” being submitted by **Mr. SHIVANSH AWASTHI** to the Indian Institute of Technology Delhi for the award of the degree of “**Doctor of Philosophy**”, is a record of bonafide research work carried out by him under my guidance and supervision.

In my opinion, the thesis has reached the standard of fulfilling the requirement of all the regulations regarding to the degree. For the award of Joint degree, the results contained in this thesis have been submitted to National Yang Ming Chiao Tung University as a part of IITD-NYCU Joint Degree Program.



Prof. Ankur Gupta

Centre for Applied Research in Electronics
Indian Institute of Technology Delhi
New Delhi- 110016,
India



Prof. Heng-Tung Hsu

Internation College of Semiconductor Technology
National Yang Ming Chiao Tung University
Hsin-Chu, 30010
Taiwan

ACKNOWLEDGEMENTS

I would first like to express my deepest gratitude to my supervisor, Prof. Ankur Gupta, for his unwavering guidance, support, and trust throughout my doctoral journey. His academic insight, constant encouragement, and the freedom he provided to explore ideas independently have shaped every stage of this research. I am especially grateful for his unwavering support during difficult phases and for extending every form of assistance, academic, financial, and personal, whenever required. He not only guided the technical aspects of this work but also taught me how to think, question, and approach research in deeper and more meaningful ways. This thesis would not have been possible without his continued mentorship and belief in my abilities.

I am equally grateful to my co-supervisor, Prof. Heng-Tung (Becker) Hsu whose technical expertise, and thoughtful guidance, have been indispensable to the progress of this work. His detailed feedback, scientific clarity, and numerous brainstorming sessions significantly enriched the direction and quality of this thesis. The contributions from Prof. Hsu have been foundational, and many aspects of this work would simply not have been possible without his involvement. My sincere thanks also go to Prof. Hsu, for providing full access to laboratory facilities and for his supportive and welcoming attitude during my time in ICST, NYCU Taiwan. His cooperation enabled several critical elements of this research.

I extend my heartfelt appreciation to my SRC members Prof. Samaresh Das, Prof. Rajendra Singh, and chairman Prof. Ananjan Basu for their valuable feedback during periodic evaluations each semester. Their insightful observations and constructive feedback consistently helped refine and strengthen my research.

I am thankful to all the faculty members of CARE IIT Delhi, research scholars, and staff in the Microelectronics and VLSI group at IIT Delhi, for creating a collaborative and supportive environment that greatly benefited my learning and research.

Special acknowledgment is due to Vikas Kumar, my lab mate and friend in IIT Delhi, for his steadfast support, technical discussions, and countless brainstorming sessions. His presence made both the scientific challenges and daily work far more manageable and enjoyable. I would also like to thank my friends and lab mates from my mm-wave lab in ICST, NYCU Taiwan, Dr. Ping Hsin Chiu (Dale), Dr Yuan Wang (Oliver), Jiun-Jie Huang (Ryan), and Chun-Yi Hsia (Iris) for their warmth and acceptance during my dual degree tenure in NYCU Taiwan. I am deeply grateful to

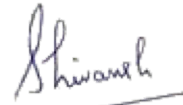
Prof. Yi-Fan Tsao (Tom) and Dr. Ping Hsin Chiu (Dale), for their continuous guidance, technical discussion, and support during my tenure in NYCU Taiwan.

My heartfelt gratitude extends to Dr. Eldad Bahat-Treidel and Prof. Joachim Würfl (FBH, Berlin, Germany) for their valuable technical discussions and for the opportunities to exchange and refine ideas during collaborative meetings at NYCU Taiwan. Their insights significantly broadened the scope of my understanding of AlGaIn/GaN HEMT.

I owe profound thanks to my father and friend, Mr. H.D. Awasthi and Mother Mrs. Alka Sharma for their unwavering love, emotional strength, and constant belief in me. Their support has carried me through the most demanding phases of this journey. I am equally grateful to my wife, Dr. Srishti Sharma, for being my closest friend and pillar of support during toughest phases of my PhD journey. I extend my deepest gratitude to my beloved grandmother (*Nani*) Mrs. Uma Sharma, whose unwavering prayers and endless blessings have been a source of strength in my journey. I would like to thank my parents-in-law and sister-in-law, Dr. Ishita, for their encouragement and understanding.

I would also like to thank my friend Akshay Sharma, along with all my school friends, for keeping me grounded and for giving me the much-needed breaks that helped me stay motivated and rejuvenated throughout my PhD.

Finally, I thank God for granting me the strength, resilience, and clarity to persevere through every stage of this journey. While my contribution to science may be modest, this journey has transformed me deeply, and for that, I am immensely grateful.



Shivansh Awasthi

Abstract

Modern wireless systems including 5G/6G transceivers, EHF radar front ends, satellite links, and emerging THz sensors require power amplifiers and receiver devices with high linearity, wide bandwidth, and strong reliability. GaN high-electron-mobility transistors (HEMTs) play a key role due to their high breakdown field, strong polarization-induced 2DEG, and ability to deliver high power at high frequencies. However, challenges such as nonlinear transconductance, hot-electron degradation, surface and buffer trapping, and dynamic reliability effects still limit linearity, gain, and current collapse. This thesis addresses these issues through coordinated device engineering, experimental reliability studies, physics-based TCAD modeling, and machine-learning-based predictive analysis.

The first part investigates electrostatic linearity engineering using a dual-gate (DG) InAlGaN/GaN HEMT architecture that improves g_m flatness and suppresses RF nonlinearities. A source-side secondary gate enhances channel modulation, reduces IMD3, and expands the linear operating range without compromising cutoff or maximum oscillation frequency. Large-signal modeling confirms improved C/I ratio and AM-PM behavior, establishing DG-HEMTs as strong candidates for highly linear RF power amplifiers and V-band front ends.

The second theme examines reliability under extreme RF operation. On-wafer tests on 0.1 μm AlGaN/GaN HEMTs under 60 GHz Class-AB RF stress for over two days and complementary DC stress for five days show stable gate leakage but significant degradation in gain, output power, and PAE, indicating RF-accelerated mechanisms not seen in DC stress alone. A calibrated TCAD reliability model incorporating hot-carrier effects, self-heating, and dynamic trap generation reproduces the degradation and reveals insights into field-induced trap activation, inverse piezoelectric field shifts, and barrier-defect impacts on long-term mm-wave reliability.

In the third part of this thesis, the potential of GaN HEMTs for non-resonant terahertz (THz) detection is investigated using advanced device structures. A dual-gate configuration is introduced to improve responsivity and noise-equivalent power (NEP), with performance compared against multi-channel HEMTs to highlight the benefits of InAlGaN barriers for

enhanced THz detection. The optimized design delivers higher responsivity and lower NEP. A reliability study incorporating trap distributions and temperature variations further confirms the robustness and practical viability of the proposed device for dependable THz detection.

The fourth phase proposes and analyzes a dual-channel graded-barrier (DCGB) GaN HEMT to address buffer-trap-induced current collapse. Transient and electro-thermal simulations show strong suppression of drain-lag degradation due to enhanced charge confinement, a 3D electron gas formed by graded polarization, and spatial decoupling of the upper channel from the Fe-doped buffer. These engineered barrier-grading and multi-channel transport effects significantly mitigate collapse mechanisms, enabling more stable high-power and high-frequency operation.

The final section introduces a machine-learning (ML) framework trained on TCAD-generated data and measured device behavior to predict intrinsic parameters such as threshold voltage (V_{TH}) and transconductance (g_m). Ensemble methods like Random Forest and Gradient Boost surpass conventional regression and match deep-learning accuracy while offering greater interpretability and efficiency. This physics-guided ML approach provides a fast, reliable route for future GaN device optimization and reliability prediction.

Collectively, this thesis provides an integrated understanding of GaN HEMT behavior across linearity, reliability, collapse suppression, THz detection potential, and data-driven modeling. The synergy between experimental measurements, advanced TCAD simulations, and predictive ML tools establishes a robust methodology for engineering next-generation GaN devices for RF, EHF, and THz applications, ultimately contributing to more efficient, reliable, and scalable wireless transceiver technologies.

सार

मॉडर्न वायरलेस सिस्टम—जिसमें 5G/6G ट्रांसीवर, EHF रडार फ्रंट एंड, सैटेलाइट लिंक और नए THz सेंसर शामिल हैं—को हाई लीनियरिटी, वाइड बैंडविड्थ और मज़बूत रिलायबिलिटी वाले पावर एम्पलीफायर और रिसीवर डिवाइस की ज़रूरत होती है। GaN हाई-इलेक्ट्रॉन-मोबिलिटी ट्रांजिस्टर (HEMTs) अपने हाई ब्रेकडाउन फील्ड, मज़बूत पोलराइजेशन-इंड्यूस्ड 2DEG और हाई फ्रीक्वेंसी पर हाई पावर देने की क्षमता के कारण अहम भूमिका निभाते हैं। हालांकि, नॉनलीनियर ट्रांसकंडक्टेंस, हॉट-इलेक्ट्रॉन डिग्रेडेशन, सरफेस और बफर ट्रैपिंग, और डायनामिक रिलायबिलिटी इफेक्ट्स जैसी चुनौतियां अभी भी लीनियरिटी, गेन और करंट कोलैप्स को सीमित करती हैं। यह थीसिस कोऑर्डिनेटेड डिवाइस इंजीनियरिंग, एक्सपेरिमेंटल रिलायबिलिटी स्टडीज़, फिजिक्स-बेस्ड TCAD मॉडलिंग और मशीन-लर्निंग-बेस्ड प्रेडिक्टिव एनालिसिस के ज़रिए इन मुद्दों को सुलझाती है।

पहला भाग डुअल-गेट (DG) InAlGa_N/Ga_N HEMT आर्किटेक्चर का इस्तेमाल करके इलेक्ट्रोस्टैटिक लीनियरिटी इंजीनियरिंग की जांच करता है जो gm प्लैटनेस को बेहतर बनाता है और RF नॉनलीनियरिटी को दबाता है। सोर्स-साइड सेकेंडरी गेट चैनल मॉड्यूलेशन को बढ़ाता है, IMD3 को कम करता है, और कटऑफ या मैक्सिमम ऑसिलेशन फ्रीक्वेंसी से समझौता किए बिना लीनियर ऑपरेटिंग रेंज को बढ़ाता है। लार्ज-सिग्नल मॉडलिंग बेहतर C/I रेश्यो और AM-PM बिहेवियर को कन्फर्म करता है, जिससे DG-HEMTs को बहुत ज़्यादा लीनियर RF पावर एम्पलीफायर और V-बैंड फ्रंट एंड के लिए मज़बूत कैंडिडेट के तौर पर स्थापित किया गया है।

दूसरी थीम बहुत ज़्यादा RF ऑपरेशन के तहत रिलायबिलिटी की जांच करती है। 0.1 μm AlGa_N/Ga_N HEMTs पर 60 GHz क्लास-AB RF स्ट्रेस के तहत दो दिनों से ज़्यादा और कॉम्प्लिमेंट्री DC स्ट्रेस के तहत पांच दिनों तक ऑन-वेफर टेस्ट से स्टेबल गेट लीकेज दिखता है, लेकिन गेन, आउटपुट पावर और PAE में काफी गिरावट आती है, जो ऐसे RF-एक्सेलरेटेड मैकेनिज्म को दिखाता है जो सिर्फ DC स्ट्रेस में नहीं दिखते। हॉट-कैरियर इफ़ेक्ट, सेल्फ़-हीटिंग और डायनामिक ट्रैप जेनरेशन को शामिल करने वाला एक कैलिब्रेटेड TCAD रिलायबिलिटी मॉडल, गिरावट को दोहराता है और फ़ील्ड-इंड्यूस्ड ट्रैप एक्टिवेशन, इनवर्स पीज़ोइलेक्ट्रिक फ़ील्ड शिफ़्ट और लंबे समय तक चलने वाली mm-वेव रिलायबिलिटी पर बैरियर-डिफ़ेक्ट के असर के बारे में जानकारी देता है।

इस थीसिस के तीसरे हिस्से में, एडवांस्ड डिवाइस स्ट्रक्चर का इस्तेमाल करके नॉन-रेज़ोनेंट

टेराहर्ट्ज़ (THz) डिटेक्शन के लिए GaN HEMTs की क्षमता की जांच की गई है। रिस्पॉन्सिविटी और नॉइज़-इक्विवेलेंट पावर (NEP) को बेहतर बनाने के लिए एक डुअल-गेट कॉन्फ़िगरेशन पेश किया गया है, जिसमें बेहतर THz डिटेक्शन के लिए InAlGaN बैरियर के फ़ायदों को हाईलाइट करने के लिए मल्टी-चैनल HEMTs के मुकाबले परफ़ॉर्मेंस की तुलना की गई है। ऑप्टिमाइज़्ड डिज़ाइन ज़्यादा रिस्पॉन्सिविटी और कम NEP देता है। ट्रैप डिस्ट्रिब्यूशन और टेम्परेचर वेरिएशन को शामिल करने वाली एक रिलायबिलिटी स्टडी, भरोसेमंद THz डिटेक्शन के लिए प्रस्तावित डिवाइस की मज़बूती और प्रैक्टिकल वायबिलिटी को और कन्फ़र्म करती है।

चौथा फेज़ बफ़र-ट्रैप से होने वाले करंट कोलैप्स को ठीक करने के लिए एक डुअल-चैनल ग्रेडेड-बैरियर (DCGB) GaN HEMT का प्रस्ताव और एनालिसिस करता है। ट्रांजिएंट और इलेक्ट्रो-थर्मल सिमुलेशन, बढ़े हुए चार्ज कन्फ़ाइनमेंट, ग्रेडेड पोलराइज़ेशन से बनी 3D इलेक्ट्रॉन गैस, और Fe-डोपड बफ़र से ऊपरी चैनल के स्पेशल डीकपलिंग के कारण ड्रेन-लैग डिग्रेडेशन को मज़बूती से दबाते हैं। ये इंजीनियर्ड बैरियर-ग्रेडिंग और मल्टी-चैनल ट्रांसपोर्ट इफ़ेक्ट कोलैप्स मैकेनिज़्म को काफ़ी कम करते हैं, जिससे ज़्यादा स्टेबल हाई-पावर और हाई-फ़्रीक्वेंसी ऑपरेशन मुमकिन होता है।

आखिरी सेक्शन एक मशीन-लर्निंग (ML) फ्रेमवर्क पेश करता है जो TCAD से बने डेटा और मापे गए डिवाइस बिहेवियर पर ट्रेन किया गया है ताकि थ्रेशोल्ड वोल्टेज (VTH) और ट्रांसकंडक्टेंस (gm) जैसे इंट्रिंसिक पैरामीटर्स का अनुमान लगाया जा सके। रैंडम फ़ॉरेस्ट और ग्रेडिएंट बूस्ट जैसे एनसेंबल मेथड पारंपरिक रिग्रेसन से आगे निकल जाते हैं और डीप-लर्निंग एक्यूरेसी से मेल खाते हैं, साथ ही ज़्यादा इंटरप्रेटेबिलिटी और एफ़िशिएंसी भी देते हैं। यह फ़िज़िक्स-गाइडेड ML अप्रोच भविष्य के GaN डिवाइस ऑप्टिमाइज़ेशन और रिलायबिलिटी अनुमान के लिए एक तेज़, भरोसेमंद रास्ता देता है।

कुल मिलाकर, यह थीसिस लीनियरिटी, रिलायबिलिटी, कोलैप्स सप्रेसन, THz डिटेक्शन पोटेन्शियल और डेटा-ड्रिवन मॉडलिंग में GaN HEMT बिहेवियर की एक इंटीग्रेटेड समझ देती है। एक्सपेरिमेंटल मेज़रमेंट, एडवांस्ड TCAD सिमुलेशन और प्रेडिक्टिव ML टूल्स के बीच सिनर्जी RF, EHF और THz एप्लीकेशन के लिए नेक्स्ट-जेनरेशन GaN डिवाइस की इंजीनियरिंग के लिए एक मज़बूत मेथडोलॉजी बनाती है, जो आखिर में ज़्यादा एफ़िशिएंट, रिलायबल और स्केलेबल वायरलेस ट्रांसीवर टेक्नोलॉजी में योगदान देती है।

CONTENTS

ACKNOWLEDGEMENTS	ii
Abstract	iv
सार	vi
LIST OF FIGURES	xii
LIST OF TABLES	xxiii
LIST OF ABBREVIATIONS	xxiv
Chapter 1: Introduction	1
1.1 GaN Material Physics and Two-Dimensional Electron Gas (2DEG) Formation	4
1.2 Evolution of RF GaN HEMT Architectures	7
1.2.1 InAlGaN Barrier HEMTs	8
1.2.2 Polarization-Graded Barrier HEMTs.....	9
1.2.3 Multi Channel HEMTs	10
1.2.4 Gate-Engineered HEMTs	11
1.3 Reliability concerns in RF GaN HEMTs	11
1.3.1 Hot-electron effects	12
1.3.2 RF Dispersion	12
1.3.3 Current Collapse and Dynamic ON-Resistance (Ron) Degradation	13
1.3.4 Surface Traps and Buffer Traps.....	13
1.3.5 Self-Heating and Electro-Thermal Feedback	14
1.3.6 High-Frequency Versus DC Reliability Tests.....	14
1.4 Motivation and Objectives	15
1.5 Thesis Organization	16
Bibliography.....	17
Chapter 2: Enhancing RF Linearity in GaN HEMTs with Dual Gate Structures ...	21
2.1 Device Structure and Computational Framework.....	24

2.1.1 Epitaxial Layer Architecture and Device Geometry	24
2.1.2 Numerical Simulation Models.....	25
2.2 Baseline Characteristics of InAlGa _N /Ga _N HEMT	27
2.2.1 Comparison with Conventional AlGa _N /Ga _N Structure	28
2.2.2 Linearity and Gate Voltage Swing (GVS) Assessment.....	28
2.3 Optimization of Dual-Gate Architecture Using Gate Voltage Swing (GVS) Analysis	30
2.4 Linearity Analysis by Polynomial Fitting.....	33
2.5 Small signal RF Performance Evaluation of Dual-Gate HEMT Architectures	35
2.6 Large-Signal RF Behavior and Linearity Assessment of Dual-Gate Architectures ..	36
2.7 Physical Mechanism Underlying Linearity Enhancement in Dual-Gate HEMTs	41
2.8 Summary	46
Bibliography.....	47
Chapter 3: Reliability Assessment of 100-nm Ga_N HEMTs Under EHF (V-Band) and DC Stress experiments	53
3.1 Device Structure, Measurement Environment, and Stress Characterization Setup ...	55
3.2 DC Stress Experiment and Device Reliability Assessment	58
3.2.1 Drain Current Monitoring Under DC Stress.....	58
3.2.2 Pre- and Post-Stress ID-VG Characteristics	59
3.3 EHF Stress Experiment and Device Reliability Assessment	61
3.3.1 Input-Power Stability and Calibration Accuracy.....	62
3.3.2 Output Power Degradation: Evidence of RF-Induced Aging.....	63
3.3.3 Stability of Gate Current Under EHF Stress	65
3.3.4 Degradation of Drain Current Under EHF Stress.....	65
3.3.5 DC Characteristics post-EHF Stress.....	66
3.4 Large-Signal Performance Degradation and Recovery Assessment.....	69
3.4.1 Fresh Device Large-Signal Performance Under Different Load Conditions	69
3.4.2 Large-Signal Power Performance Degradation under DC and EHF Stress	72
3.5 Summary	77

Bibliography.....	77
Chapter 4: Reliability And Degradation Analysis for GaN HEMT Under EHF Stress	81
4.1 ON-State Step-Stress Test for Determining Critical Breakdown Voltage.....	83
4.2 Simulation Setup and Calibration with measured data.	88
4.3 Degradation and Failure Analysis	91
4.4 Summary	96
Bibliography.....	96
Chapter 5: Modeling and Reliability Analysis of InAlGa_N/Ga_N HEMT Based Non-resonant HEMTs THz Detectors	99
5.1 THz detection mechanism and Simulation	101
5.2 THz detection performance and Reliability Analysis	106
5.2.1 THz detection by ADG-InAlGa _N /Ga _N HEMT.....	106
5.2.2 THz detection by MC-HEMT.....	113
5.3 Summary	124
Bibliography.....	126
Chapter 6: Mitigation of Buffer Trap Induced Current Collapse in GaN HEMTs Using Graded-Barrier Structures	130
6.1 Device structure and model calibration.....	132
6.2 Structural Design and Electrostatic Characteristics of the Dual-Channel Graded-Barrier HEMT.....	134
6.3 Transient Simulation Framework for Drain-Lag and Pulse I-V Analysis	139
6.3.1 Effect of Fe Doping on Drain-Lag Transients.....	143
6.3.2 Impact of Pulse Amplitude on Drain-Lag Transients.....	144
6.4 Physical Insight into Trap Dynamics and Electric-Field Distribution	146
6.5 Summary	149
Bibliography.....	150
Chapter 7: Machine Learning based modeling of GaN HEMT for threshold voltage	

prediction	153
7.1 DC, RF and noise measurements of AlGa _N /Ga _N HEMT structure	155
7.2 ML implementation, Data processing and models description	160
7.2.1 Data Preprocessing and Standardization	161
7.2.2 Model Selection and Rationale.....	162
7.3 TCAD–ML Modeling Prediction Results and Performance Evaluation (R ² values)	164
7.4 Summary	170
Bibliography.....	171
Chapter 8:	174
Conclusions And Future Scope	174
List of Publications.....	178
Bio Data.....	181

LIST OF FIGURES

Figure 1.1: Block-level diagram of a modern wireless transceiver system showing key RF front-end components. III–V/GaN HEMTs enable the high-power amplifier (PA) on the transmit side. 1

Figure 1.2: Wurtzite crystal structure of GaN highlighting the Ga-face orientation and the inverse asymmetric stacking of Ga and N atoms. The inherent lack of inversion symmetry gives rise to strong spontaneous polarization, a fundamental property enabling 2DEG formation in GaN-based heterostructures [12]. 3

Figure 1.3 : Schematic cross-section of an AlGa_N/Ga_N HEMT illustrating the origin of spontaneous polarization in wurtzite Ga_N and piezoelectric polarization induced by tensile strain in the AlGa_N barrier. The combined polarization fields drive electron accumulation at the heterointerface, enabling channel formation without intentional doping [12]. 4

Figure 1.4: Conduction band diagram of an AlGa_N/Ga_N heterostructure showing the formation of the polarization-induced two-dimensional electron gas (2DEG). The sharp band discontinuity at the interface creates a triangular quantum well that confines electrons to form a high mobility 2DEG channel essential for HEMT operation. 5

Figure 1.5: InAlGa_N/AlN/GaN HEMT structure. 8

Figure 1.6: InAlGa_N/AlN/GaN HEMT graded barrier structure. 9

Figure 1.7: AlGa_N/AlN/GaN HEMT multi-channel structure. 10

Figure 1.8: Schematic depiction of trap states in an AlGa_N/Ga_N HEMT, showing donor-like surface/interface traps in the cap/AlGa_N region and deep acceptor-type buffer traps commonly introduced by Fe-doping in semi-insulating Ga_N buffers. Both surface (2) and buffer traps (1) influence 2DEG density, channel mobility, and dynamic reliability, contributing to phenomena such as current collapse and RF dispersion [18]. 12

Figure 2.1 Epitaxial layer structure of the InAlGa_N/AlN/GaN HEMT used for model calibration. (b) Measured [41] and simulated transfer characteristics along with the corresponding transconductance curves at a drain bias of $V_{DS} = 5V$, showing good agreement between experiment and TCAD model. 25

Figure 2.2: Schematic of the proposed dual-gate HEMT configurations: (a) DG-GD structure with the additional gate near the drain, and (b) DG-GS structure with the additional gate near the source,

aimed at enhancing device linearity.....	29
Figure 2.3: (a) I_D - V_G characteristics of the proposed dual-gate HEMT structures, and (b) corresponding transconductance (g_m) profiles highlighting the effect of the dual-gate configuration on device performance.....	29
Figure 2.4: (a) I_D - V_D characteristics of the SG HEMT structures, and (b and c) proposed Dual posed dual-gate source-side (DG-GS) configuration, and proposed dual gate drain side DG (G-D) configuration.....	31
Figure 2.5: Simulated gate-voltage swing (GVS) plotted against DC gate bias for several inter-gate spacings dG in (a) the drain-side dual-gate (DG-GD) structure and (b) the source-side dual-gate (DG-GS) structure, highlighting the distinct sensitivity of both configurations to dG	32
Figure 2.6: (a) Extracted cutoff frequency (f_T) and (b) maximum oscillation frequency (f_{max}) for the single-gate (SG), drain-side dual-gate (DG-GD), and source-side dual-gate (DG-GS) InAlGaIn/GaN HEMT structures. (c) Small-signal current-gain characteristics used to determine f_T , and (d) maximum-power-gain plots used for f_{max} extraction. The DG-GS architecture maintains RF performance close to the SG device, exhibiting only marginal reduction in high-frequency figures of merit.....	35
Figure 2.7: Simulated large-signal behavior of the developed HEMT models at 28 GHz for (a) single-gate (SG), (b) dual-gate near drain (DG-GD), and (c) dual-gate near source (DG-GS) configurations, showing the impact of gate design on output characteristics.....	37
Figure 2.8: Simulated (a) AM–AM and (b) AM–PM conversion characteristics comparing the SG, DG-GS, and DG-GD devices, highlighting the reduction in gain and phase distortion achieved by the dual-gate architectures.....	38
Figure 2.9: Extracted C_{GS} versus V_{GS} characteristics for the SG, DG-GS, and DG-GD HEMTs, illustrating the reduced voltage dependence of C_{GS} in the dual-gate design.....	38
Figure 2.10: Comparison of the carrier-to-intermodulation (C/I) ratio for the SG, DG-GS, and DG-GD HEMTs, evaluated using a two-tone excitation at 28 GHz to assess third-order nonlinear distortion.....	39
Figure 2.11: EVM characteristics of the SG, DG-GS, and DG-GD configurations at 38 GHz, showing the variation of modulation accuracy with output power.....	40
Figure 2.12: Simulated second derivative of the electron velocity along the channel for various gate voltages in SG, DG-GD, and DG-GS configurations: (a-c) show the source-to-gate access	

region, and (d-f) depict the gate-to-drain access region, illustrating the effect of dual-gate placement on channel electron dynamics. 42

Figure 2.13: Simulated electron current density profiles for the SG and DG–GS configurations at three characteristic gate voltages: (a) $V_{GS} = V_1$ marking the lower end of the GVS interval, (b) $V_{GS} = V_{gm,max}$ corresponding to the peak transconductance, and (c) $V_{GS} = V_2$ representing the upper end of the GVS interval. (d) The transconductance curve highlighting these bias points relative to the extracted GVS and peak gm . ($V_{gm,max} = -1.9$ V for DG-GS and -2.1 V for SG; $V_1 = -2.7$ V for both devices; $V_2 = 0.8$ V for DG GS and -0.39 V for SG). 43

Figure 2.14: Simulated conduction band diagrams for the DG-GS dual-gate and single-gate HEMT structures. The energy band profiles are extracted along a cutline located underneath the RF gate to highlight the differences in channel potential modulation. 44

Figure 3.1: Measurement setup used for EHF stress experiments on $0.1 \mu\text{m}$ GaN HEMT. 56

Figure 3.2: Drain current evolution during 120-hour DC stress test at $V_{DS} = 12$ V showing negligible variation throughout the five-day stress period, indicating excellent current stability and absence of DC-induced degradation. 58

Figure 3.3: Measured I_D - V_{GS} characteristics at $V_{DS} = 2, 4, 6,$ and 8 V before and after 120-hour DC stress, showing identical threshold voltage, slope, and maximum current, confirming no DC-induced degradation in transfer characteristics. 59

Figure 3.4: Comparison of pre- and post-stress transconductance (g_m) characteristics showing identical peak values, curve shape, and voltage position, confirming absence of mobility degradation or threshold shift under DC stress. 60

Figure 3.5: Evolution of the monitored input power during the three 60-hour EHF stress experiments at $P_{1dB}, P_{2dB},$ and P_{3dB} drive levels. The high stability of the input RF power confirms a reliable and drift-free measurement environment. 63

Figure 3.6: Time-dependent large-signal output power (P_{out}) degradation during the 60-hour EHF stress experiment. Output power decreases progressively with higher drive levels, with maximum degradation of ~ 0.9 dB at P_{3dB} , indicating strong RF-induced aging. 64

Figure 3.7: Gate current (I_G) monitored during the 60-hour EHF stress test for $P_{1dB}, P_{2dB},$ and P_{3dB} conditions. The consistent and stable I_G indicates the absence of gate leakage increase or Schottky barrier degradation. 65

Figure 3.8: Drain current (I_D) degradation during 60-hour EHF stress. The current decreases by

11%, 15%, and 21% at P_{1dB} , P_{2dB} , and P_{3dB} , respectively, demonstrating the strong influence of RF-induced trapping and channel mobility reduction.	66
Figure 3.9: Measured transfer characteristics (I_D-V_{GS}) of the 0.1- μm AlGaIn/GaN HEMT before and after 60-hour EHF stress at P_{3dB} . A slight reduction in drain current is visible, but no meaningful shift in V_{TH} is observed, confirming the absence of permanent threshold-related degradation.....	67
Figure 3.10: Extracted transconductance (g_m) profiles of the device before and after EHF stress. The peak g_m value and its position along the V_{GS} axis remain nearly identical, confirming that mobility degradation or permanent RF-induced damage does not manifest during DC operation.	68
Figure 3.11: Measured large-signal performance of the fresh AlGaIn/GaN HEMT with the load tuned for maximum output power under Class-AB operation.....	70
Figure 3.12 : Large-signal P_{out} , gain, and PAE before and after 60 hours of DC stress. The overlapping curves confirm that DC stress does not cause any measurable performance degradation.....	72
Figure 3.13: Large-signal characteristics before and after EHF stress at the P_{1dB} input power level. Mild reductions in P_{out} , gain, and PAE underline the onset of RF-specific degradation mechanisms.....	73
Figure 3.14: Large-signal performance before and after P_{2dB} EHF stress. Degradation becomes more pronounced, revealing clear field-dependent deterioration of device behavior.	73
Figure 3.15: Large-signal performance before and after P_{3dB} EHF stress. Significant and irreversible degradation is observed, with marked reduction in P_{out} , PAE, and gain after stress and no recovery after four weeks.....	74
Figure 4.1: OFF-state gate leakage current and corresponding change in maximum drain current ($\Delta I_D, \max$) extracted from DC ON-state step-stress for the fresh device, showing the onset of inverse piezoelectric degradation at $V_{DG} \approx 15$ V.	85
Figure 4.2: ON-state step-stress measurement after EHF stress at P_{1dB} . The critical V_{DG} remains unchanged at ~ 15 V.	86
Figure 4.3: ON-state step-stress measurement after EHF stress at P_{2dB} . The critical V_{DG} remains unchanged at ~ 15 V.	86
Figure 4.4: ON-state step-stress measurement after EHF stress at P_{3dB} . The critical V_{DG} remains	

unchanged at ~15 V.	87
Figure 4.5: Calibration of the simulated I_D - V_G characteristics with measured data for the 0.1- μm AlGaIn/GaN HEMT, demonstrating excellent agreement in threshold voltage, transconductance, and current levels.	89
Figure 4.6: Measured and simulated transfer characteristics (I_D - V_G) of the 0.1- μm AlGaIn/GaN HEMT, demonstrating excellent agreement between experiment and TCAD results. The curves in blue illustrate the reduction in drain current reproduced through the introduction of acceptor-like barrier traps. Inset: mixed-mode simulation setup used to model EHF-induced degradation.	90
Figure 4.7: Simulated lateral electric field beneath the channel in the gate-drain access region before and after EHF stress. A pronounced field spike develops after $P3\text{dB}$ stress, indicating strong field crowding and hot-electron activation. Inset: cutline location used for electric field extraction.	91
Figure 4.8: Simulated electric field distribution in the AlGaIn/GaN HEMT structure: (a) epitaxial stack, (b) fresh device, (c) after $P1\text{dB}$ stress, and (d) after $P3\text{dB}$ stress. The field evolution highlights progressive intensification and localization of the high-field region under increasing RF stress, with the most severe crowding observed after $P3\text{dB}$ excitation.	92
Figure 4.9: Post-stress ionized acceptor trap density in the AlGaIn barrier and GaN buffer: (a) fresh device, (b) after $P1\text{dB}$ stress, and (c) after $P3\text{dB}$ stress. The higher trap occupation after $P3\text{dB}$ stress indicates deep-level activation and barrier degradation responsible for the measured current collapse.	93
Figure 4.10: Simulated lattice temperature distribution following EHF stress: (a) contour plot showing a localized thermal hotspot near the drain-side gate edge, and (b) temperature profile along the channel extracted along the indicated cutline. The hotspot formation correlates with enhanced hot-electron activity and contributes to irreversible trap generation.	94
Figure 5.1: (a) Schematic of the simulated single-channel asymmetric dual-gate (SC-ADG) InAlGaIn/GaN HEMT illustrating the primary sensing gate and the independently biased auxiliary gate. (b) Corresponding conduction-band profile extracted along the channel, highlighting 2DEG confinement in the SC-ADG structure. (c) Structural layout of the multi-channel (MC) AlGaIn/GaN HEMT, showing the vertically stacked barrier layers used to form multiple 2DEG sheets. (d) Simulated energy-band diagram for the MC-HEMT device, demonstrating enhanced charge confinement arising from the dual-barrier architecture.	102

Figure 5.2: (a) Mixed-mode TCAD configuration used to emulate non-resonant THz detection, where an AC excitation is applied at the gate and the rectified output is monitored at the drain through the load resistor RL .(b) Time-domain waveform of the drain-side response voltage, illustrating the rectification behavior generated by the incident 0.9-THz signal.(c) Frequency-spectrum of the simulated response obtained using FFT analysis, clearly showing a dominant peak at the excitation frequency of 0.9 THz, confirming correct coupling and detection within the device. 105

Figure 5.3: Transfer characteristics and rectified THz response of the SC-ADG InAlGa_n/Ga_n HEMT under varying indium composition. Increasing indium fraction reduces channel current due to enhanced alloy scattering, while the THz response ΔU remains largely unchanged, indicating weak dependence of detection sensitivity on barrier composition. 107

Figure 5.4: Drain current and THz response as functions of Gate-2 bias in the ADG-InAlGa_n/Ga_n HEMT. A strong enhancement in ΔU is obtained near $V_{G2} = 4$ V due to increased channel-potential asymmetry, while the drain current remains nearly constant over the applied bias range. 108

Figure 5.5: I_D - V_G characteristics and THz response of the multichannel AlGa_n/Ga_n HEMT for different top-barrier thicknesses. Optimization of the barrier thickness reveals an operating point that maximizes ΔU while preserving adequate channel conduction for THz detection applications. 109

Figure 5.6: (a) Extracted responsivity (R_v) showing a pronounced peak at the optimized secondary-gate bias of 4 V, enabled by enhanced electrostatic asymmetry and improved nonlinear rectification efficiency. (b) Corresponding Noise-Equivalent Power (NEP), which reaches a minimum near 80 pW/Hz^{0.5} at the same bias condition, demonstrating the high sensitivity and low-noise operation of the quaternary-barrier SC-ADG HEMT under non-resonant THz excitation. 110

Figure 5.7: : Temperature-dependent THz detection performance of the optimized SC-ADG InAlGa_n/Ga_n HEMT detector (a) Variation of responsivity as the ambient temperature increases from 25 °C to 200 °C, showing a gradual reduction in rectified output due to thermally enhanced scattering and weakened field asymmetry. (b) Corresponding evolution of the Noise-Equivalent Power (NEP), which increases with temperature as responsivity decreases, reflecting the device’s sensitivity degradation at high temperatures. These results collectively demonstrate the thermal limits and robustness of the quaternary-barrier SC-ADG detector under elevated operating

temperatures.....	112
Figure 5.8: Baseline DC characteristics of the multi-channel GaN HEMT under varying top AlGaIn barrier (AlGaIn-1) thickness. (a) Transfer characteristics (I_D - V_G) showing the influence of barrier thickness on channel formation and 2DEG density. (b) Corresponding transconductance (g_m - V_G) profiles illustrating changes in gate coupling and carrier transport with increasing AlGaIn-1 thickness.....	114
Figure 5.9: Baseline electrical characteristics of the multi-channel HEMT structure for various GaN-1 (upper channel) thicknesses. (a) I_D - V_G curves illustrating the impact of GaN-1 thickness on threshold voltage and channel conduction. (b) Corresponding g_m - V_G characteristics highlight changes in carrier modulation efficiency as the top-channel thickness is varied.	115
Figure 5.10 : Effect of access-region geometry on the multi-channel HEMT transconductance. (a) g_m - V_G characteristics for different gate-source (L_{GS}) spacings. (b) $g_m=0$ - V_G characteristics for different gate-drain (L_{GD}) spacings, demonstrating the sensitivity of transconductance to source-side design while showing minimal dependence on drain-side variations.	116
Figure 5.11: Influence of surface donor trap density on the response voltage of the multi-channel HEMT THz detector. The figure illustrates how variations in surface trap concentration modify the channel charge environment and affect the self-mixing-based THz rectification process. ..	117
Figure 5.12: Effect of buffer trap density on the response voltage of the multi-channel HEMT THz detector. The plot highlights the sensitivity of the detector output to traps located in the semi-insulating GaN buffer and their role in modulating channel charge and threshold voltage.	118
Figure 5.13: Simulated transient THz-induced drain voltage response $V_{DS}(t)$ for single-channel (SC) and multi-channel (MC) HEMT detectors at a buffer trap density of $5 \times 10^{16} \text{ cm}^{-3}$, highlighting the intrinsically stronger rectification sustained by the MC structure.	119
Figure 5.14: Transient $V_{DS}(t)$ response of the MC-HEMT detector for buffer trap densities ranging from 5×10^{16} to $1 \times 10^{18} \text{ cm}^{-3}$, demonstrating the architecture's resilience to trap activation and the preservation of THz rectification due to its vertically decoupled channel system	121
Figure 5.15: $V_{DS}(t)$ response of the SC-HEMT detector under increasing buffer trap densities (5×10^{16} - $1 \times 10^{18} \text{ cm}^{-3}$), showing pronounced degradation and substantial suppression of the rectified output as trapping intensifies in the buffer region.	121
Figure 5.16: Simulated electric-field distribution in the SC-HEMT and MC-HEMT structures at a buffer-trap density of $5 \times 10^{16} \text{ cm}^{-3}$, highlighting differences in field localization, vertical field	

spreading, and channel–trap interaction.	123
Figure 5.17 : Spatial distribution of ionized acceptor traps in the SC-HEMT and MC-HEMT architectures at a trap density of $5 \times 10^{16} \text{ cm}^{-3}$, illustrating the contrasting trap activation patterns and the shielding effect offered by the upper channel in the MC device.	124
Figure 6.1: (a) Cross-sectional schematic of the AlGa _N /Ga _N HEMT structure used for model calibration, showing the epitaxial stack and lateral geometry.	133
Figure 6.2: (a) Comparison of simulated and experimentally measured characteristics [16], including the transfer curve at $V_{DS} = 10 \text{ V}$ and (b) output characteristics for gate biases from -3.5 V to 0 V . The excellent agreement verifies the accuracy of the calibrated TCAD model used in this work.....	134
Figure 6.3: Cross-sectional schematic of the proposed dual-channel graded-barrier InAlGa _N /Ga _N HEMT. The structure incorporates a quaternary InAlGa _N top barrier, a polarization-graded AlGa _N layer (0 to 30 %), and two Ga _N channel layers, grown on a Fe-doped Ga _N buffer over a SiC substrate. Key lateral dimensions include $LG = 250 \text{ nm}$, $LGS = 0.8 \mu\text{m}$, and $LGD = 2.7 \mu\text{m}$. ..	135
Figure 6.4: Simulated conduction band profile of the graded-barrier dual-channel InAlGa _N /Ga _N HEMT, showing formation of a 3DEG at the graded AlGa _N /Ga _N interface and a high-density 2DEG under the InAlGa _N top barrier.....	136
Figure 6.5: DC transfer characteristics comparing the single-channel InAlGa _N /Ga _N HEMT with the proposed dual-channel graded-barrier InAlGa _N /Ga _N HEMT. The DCGB architecture exhibits higher drain current and a shifted threshold voltage due to increased channel charge.....	137
Figure 6.6: Transfer characteristics of DCGB HEMTs employing either an AlGa _N or an InAlGa _N top barrier. The InAlGa _N -based structure shows superior current drive and improved threshold behavior due to lattice matching and enhanced polarization charge.	138
Figure 6.7: Mixed-mode transient simulation configuration used to evaluate drain-lag behaviour. A fast drain-voltage pulse is applied while maintaining the gate at $V_{GS} = 0 \text{ V}$ to isolate buffer-trap dynamics. The pulse features 10-ns rise and fall times to capture rapid carrier-trapping transients.	139
Figure 6.8: Comparison between simulated and experimentally measured [16] drain-lag transients. The drain current response to a $0\text{--}5 \text{ V}$ pulse (10-ns rise/fall, 1-ms width) at $V_{GS} = 0 \text{ V}$ demonstrates accurate calibration of trap-induced capture and emission dynamics in the Fe-doped Ga _N buffer.	140

Figure 6.9 : Comparison Drain-lag transients of GaN HEMTs under varying Fe-doping concentrations for (a) InAlGa_N/Ga_N single-channel (SC), (b) AlGa_N/Ga_N SC, (c) InAlGa_N/Ga_N dual-channel graded-barrier (DCGB), d (d) AlGa_N/Ga_N DCGB devices. Each device is subjected to a drain-voltage pulse rising from 5 V to 20 V, with $V_{GS} = 0V$, to isolate buffer-trap–induced current dispersion..... 142

Figure 6.10: Post-stress recovery ratio of drain-lag current as a function of Fe-trap density for SC and DCGB devices. The metric quantifies the fraction of drain current restored after the pulse, revealing the sensitivity of each architecture to deep acceptor-state occupation. 144

Figure 6.11: Impact of pulse amplitude on drain-lag transients for (a) InAlGa_N/Ga_N SC, (b) AlGa_N/Ga_N SC, (c) InAlGa_N/Ga_N DCGB, and (d) AlGa_N/Ga_N DCGB structures. The drain voltage is stepped from 5 V up to the corresponding $V_{D,max}$ to evaluate collapse severity under high-field excitation. 145

Figure 6.12: Recovery ratio of drain-lag transients as a function of the applied pulse amplitude for SC and DCGB devices. Higher stress voltage amplifies trap activation and quantifies the resilience of dual-channel graded-barrier design. 146

Figure 6.13: Simulated lateral electric-field contours for (a) the single-channel InAlGa_N/Ga_N HEMT and (b) the dual-channel graded-barrier (DCGB) InAlGa_N/Ga_N HEMT under identical drain-bias conditions. The DCGB structure exhibits a significantly redistributed and reduced peak electric field in the gate–drain access region owing to polarization grading and dual-channel field spreading. 147

Figure 6.14 : Ionized acceptor-trap density maps for (a) the SC InAlGa_N/Ga_N HEMT and (b) the DCGB InAlGa_N/Ga_N HEMT simulated at a buffer-trap concentration of $2 \times 10^{19} \text{ cm}^{-3}$. The DCGB device shows markedly suppressed trap activation in the conduction path due to vertical carrier partitioning between the upper and lower channels. Energy band diagrams extracted below the gate at the drain-side edge for (c) SC and (d) DCGB InAlGa_N/Ga_N HEMTs, illustrating the band modulation before and after the drain stress pulse ($t = t_p +$). 148

Figure 7.1: Optical image of the AlGa_N/Ga_N HEMT showing the GSG pad layout designed for on-wafer RF probing..... 156

Figure 7.2: Lakeshore probe station and Keithley 4200A-SCS analyzer used for DC measurements of transfer and output characteristics. 156

Figure 7.3: Cascade Summit 11000 probe station integrated with an Agilent E8361C PNA for

broadband S-parameter measurements up to 67 GHz.....	157
Figure 7.4: Noise Figure Analyzer (Keysight N8975B) configured with the RF probe station for microwave noise characterization up to 26 GHz.	157
Figure 7.5: (a) Measured I_{DS} - V_{GS} characteristics of the AlGaIn/GaN HEMT. (b) Corresponding transconductance (g_m) extracted from the transfer curve.....	158
Figure 7.6: Measured S21 gain of the HEMT from 100 MHz to 50 GHz for multiple drain biases, illustrating bias-dependent RF transmission behavior.....	158
Figure 7.7: Dependence of S21 on gate voltage for frequencies ranging from 1 GHz to 40 GHz, highlighting the effect of channel charge modulation.	159
Figure 7.8: Measured (c) gain and (b) noise figure of the device from 2 GHz to 10 GHz illustrating the noise performance under typical RF bias conditions.	159
Figure 7.9: Process flow illustrating the complete machine-learning pipeline used in this work, including data generation, preprocessing, model training, prediction, and validation.	161
Figure 7.10: Conceptual representation of the Random Forest [16] regressor used in this thesis, showing multiple decorrelated decision trees, whose mean output forms the final prediction. .	163
Figure 7.11: Illustration of the Gradient Boosting workflow in which successive weak learners are trained on residual errors using gradient-descent updates to improve prediction accuracy. .	163
Figure 7.12: Set of scatter plots comparing predicted and actual values of V_{TH} and g_m for each ML model, along with their corresponding coefficients of determination (R^2). These plots offer a direct visual assessment of the predictive fidelity of each method.....	165
Figure 7.13: Normalized coefficients of the Ridge regression model used for threshold-voltage prediction, highlighting the relative influence of material and structural parameters.	166
Figure 7.14: Relative importance of structural parameters for threshold-voltage prediction extracted from the trained Random Forest model.....	167
Figure 7.15: Feature-importance distribution for transconductance prediction, indicating enhanced sensitivity to lateral dimensions and barrier thickness.	167
Figure 7.16: Architecture of the multilayer ANN developed for predicting V_{TH} and g_m , comprising four hidden layers with ReLU activation.....	168
Figure 7.17: ANN performance evaluation through scatter plots and corresponding training/validation loss curves for threshold voltage and transconductance.	168
Figure 7.18: Comparison of model-predicted values with TCAD-simulated V_{TH} and g_m for Ridge	

regression, Random Forest, Gradient Boosting, and ANN, illustrating the improved agreement obtained from ensemble and deep-learning models..... 169

Figure 7.19: Performance comparison of all ML models for predicted threshold voltage and transconductance, highlighting the superior accuracy of ensemble-based methods relative to linear regression approaches. 169

LIST OF TABLES

Table 1.1: Summary of Key Material Parameters of Si, GaAs, SiC and GaN	2
Table 2.1 Numerical Models and Device Parameters used in TCAD Simulations.....	26
Table 2.2 Comparison of the Simulated DC and RF Performance of SG-AlGaN- and InAlGaN based HEMTs.....	28
Table 2.3 Comparison of DC Characteristics of Single Gate and Dual Gate Structures, along with the Extracted Coefficients.....	34
Table 3.1: Variation of threshold voltage (ΔV_{TH}) calculated at drain current of 10mA/mm before and after P_{3dB} stress.....	67
Table 3.2: Large-signal performance of the fresh device under different load conditions	70
Table 7.1: List of varied parameters to create ML Dataset.....	161

LIST OF ABBREVIATIONS

HEMT	High Electron Mobility Transistor
RF	Radio Frequency
2DEG	Two-Dimensional Electron Gas
EHF	Extremely High Frequency
GaN	Gallium Nitride
SiC	Silicon Carbide
InAlGaN	Indium Aluminium Gallium Nitride
AlGaN	Aluminium Gallium Nitride
Thz	Terahertz
AlN	Aluminium Nitride
DC	Direct Current
TCAD	Technology Computer Aided Design
ML	Machine Learning
ANN	Artificial Neural Network
GVS	Gate Voltage Swing
MC-HEMT	Multi-Channel HEMT
ADG-HEMT	Asymmetric Dual Gate HEMT